PLANETARY SCIENCE

Shock compression of stishovite and melting of silica at planetary interior conditions

M. Millot,[1,2]* N. Dubrovinskaia,[3] A. Černok,[4] S. Blaha,[4] L. Dubrovinsky,[4] D. G. Braun,[1] P. M. Celliers,[1] G. W. Collins,[1] J. H. Eggert,[1] R. Jeanloz[2]

Deep inside planets, extreme density, pressure, and temperature strongly modify the properties of the constituent materials. In particular, how much heat solids can sustain before melting under pressure is key to determining a planet's internal structure and evolution. We report laser-driven shock experiments on fused silica, α-quartz, and stishovite yielding equation-of-state and electronic conductivity data at unprecedented conditions and showing that the melting temperature of SiO_2 rises to 8300 K at a pressure of 500 gigapascals, comparable to the core-mantle boundary conditions for a 5–Earth mass super-Earth. We show that mantle silicates and core metal have comparable melting temperatures above 500 to 700 gigapascals, which could favor long-lived magma oceans for large terrestrial planets with implications for planetary magnetic-field generation in silicate magma layers deep inside such planets.

Understanding the structure, formation, and evolution of giant planets and extrasolar terrestrial planets (super-Earths) discovered to date requires knowledge of the properties of basic constituents such as iron, magnesium oxide, and silica at the relevant extreme conditions, including pressures of 100s to 1000s of GPa. Melting is arguably the most important process determining the physical and chemical evolution of planetary interiors, as differentiation of a terrestrial planet into a dense metallic core surrounded by rocky mantle and atmosphere proceeds by gravitational separation of a liquid phase (*1*). Moreover, giant impacts during the terminal stages of planetary formation can cause large-scale melting and generate a magma ocean encompassing much of the planet's rocky constituents (*2*, *3*). As mantle viscosity typically increases by more than 10 to 15 orders of magnitude upon solidification (*4*), the potential freezing of this magma ocean would greatly influence the planet's subsequent thermal evolution, geochemistry, and magnetic field.

We used shock compression of fused silica, α-quartz, and stishovite to document the pressure-density-temperature equation-of-state and optical properties (hence, electronic conductivity) of SiO_2. Stishovite's high initial density allowed us to access unprecedented high densities, which extended the experimental melting line of SiO_2 to more than 500 GPa. In combination with melting data for other oxides and iron, the high-pressure measurements provide constraints on the thermal structure and evolution of rocky planets and provide a benchmark for future theoretical (e.g., first-principles molecular dynamics), as well as experimental studies.

We used a TW-power laser pulse to send a strong, but decaying, shock through a planar target assembly (Fig. 1, A and B) (*5*). Nanosecond streaked optical pyrometry (SOP) and Doppler velocity interferometry (VISAR) recorded the shock-front velocity, reflectivity, and thermal emission as a function of time (Fig. 1, C and D). We applied impedance matching to obtain pressure-density data up to 2.5 TPa along the locus of shock (Hugoniot) states of stishovite (Fig. 2A and fig. S7). Then, following the decay of the compression wave as it traveled through the target, we obtained continuous measurements of the temperature T and reflectivity R as a function of the shock velocity U_S along the Hugoniot for three different starting materials: stishovite, α-quartz, and fused silica (initial densities of 4.29, 2.65, and 2.20 g/cm^3) (Fig. 2, B and C). Using pressure-density Hugoniot data to associate shock velocities with pressure, density, and internal energy, we can then relate the measured shock temperatures along the three Hugoniots with their respective pressure, density, and internal energy.

Shock temperature rises with increasing pressure to accommodate the increase of internal energy in excess of the compression work, in the absence of phase transitions or chemical reaction: Kinks in the temperature versus pressure are due to latent heat associated with phase changes. Our data for fused-silica and α-quartz (figs. S8 and S9 and Fig. 3A) match well with previous observations of temperature reversals (*6*–*9*) and sound speed discontinuities upon melting near 70 and 120 GPa (*10*). In addition, we observed a shock temperature plateau at 8300 ± 300 K and 500 ± 30 GPa along the stishovite Hugoniot (Figs. 2B and 3A) that we interpret as melting: an interpretation supported by previous shock data (*6*, *7*, *9*, *11*), static compression experiments at lower pressure (*12*, *13*), as well as qualitative velocimetry signatures that differentiate shock breakouts from solid and liquid silica (fig. S10). We fit the dynamic compression data and the coesite-stishovite–liquid silica triple point from static compression (*14*) (Fig. 3A), using Simon's equation (*5*) obtaining the temperature (T_m) (in Kelvins) as a function of the melting pressure (P_m) (in GPa), $T_m = 1968.5 + 307.8\ P_m^{0.485}$.

The onset of optical reflectivity when silica is shock compressed above ~10,000 K along the stishovite Hugoniot (Fig. 2C) reveals the transition to an electrically conducting state. Electronic conductivities estimated with a Drude model and assuming a strong-scattering regime (Ioffe-Regel

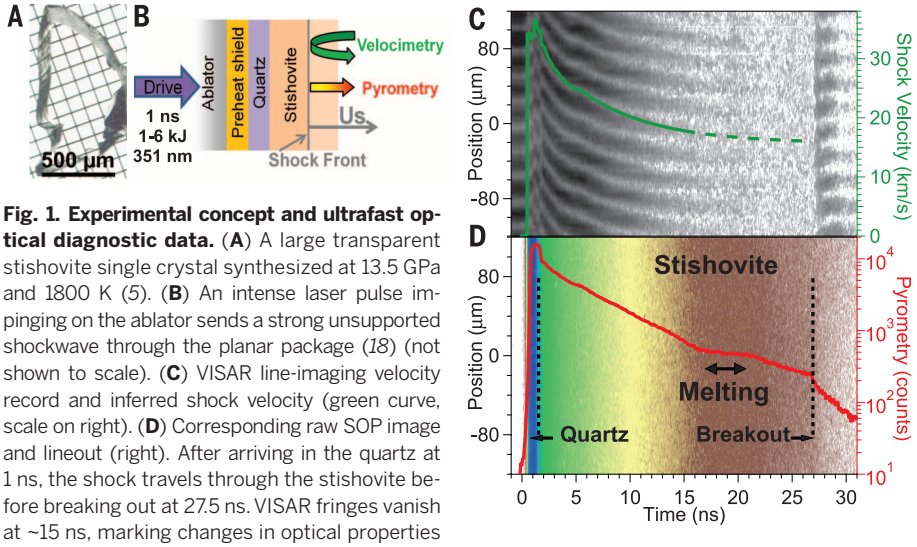

Fig. 1. Experimental concept and ultrafast optical diagnostic data. (**A**) A large transparent stishovite single crystal synthesized at 13.5 GPa and 1800 K (*5*). (**B**) An intense laser pulse impinging on the ablator sends a strong unsupported shockwave through the planar package (*18*) (not shown to scale). (**C**) VISAR line-imaging velocity record and inferred shock velocity (green curve, scale on right). (**D**) Corresponding raw SOP image and lineout (right). After arriving in the quartz at 1 ns, the shock travels through the stishovite before breaking out at 27.5 ns. VISAR fringes vanish at ~15 ns, marking changes in optical properties associated with the threshold in electrical conductivity. Melting is evident from a thermal anomaly attributed to latent heat and seen here as a change in the decay of the Hugoniot temperature and the recovery of VISAR fringes upon breakout into vacuum (*5*).

[1]Lawrence Livermore National Laboratory, Livermore, CA 94550, USA. [2]University of California Berkeley, Berkeley, CA 94720, USA. [3]Material Physics and Technology at Extreme Conditions, Laboratory of Crystallography, University of Bayreuth, 95440 Bayreuth, Germany. [4]Bayerisches Geoinstitut, University of Bayreuth, 95440 Bayreuth, Germany.
*Corresponding author. E-mail: millot1@llnl.gov

limit) increase with temperature to ~5 × 10^5 S/m and approach predicted values for liquid iron at TPa pressures ~10^6 S/m (*15*) (fig. S12). Such high values of electrical conductivity imply that liquid silicates could contribute to dynamo generation of magnetic fields inside large planets (*16*).

Dense liquid silica is also found to have an anomalously high specific heat right above the melting point (fig. S13). The shock temperature along the stishovite Hugoniot increases at a slower rate than predicted by the ANEOS model, which is based on the classical Dulong-Petit limit for the specific heat: $C_V = 3nTk_B$, where n is the number of ions and k_B is the Boltzmann constant (*9*, *17*, *18*). This reveals additional degrees of freedom in the fluid, possibly including both configurational and electronic contributions. The emergence of a complex, polymeric fluid right above the melting temperature may offer one explanation (*9*, *18*).

In combination with other recent measurements (*19*), we therefore conclude that silica and magnesium oxide are solid in the deep interior of icy giants like Uranus and Neptune, as well as—with extrapolation—in the rocky core of Saturn and Jupiter (Fig. 3B). This is particularly interesting as silicates are expected to dissociate

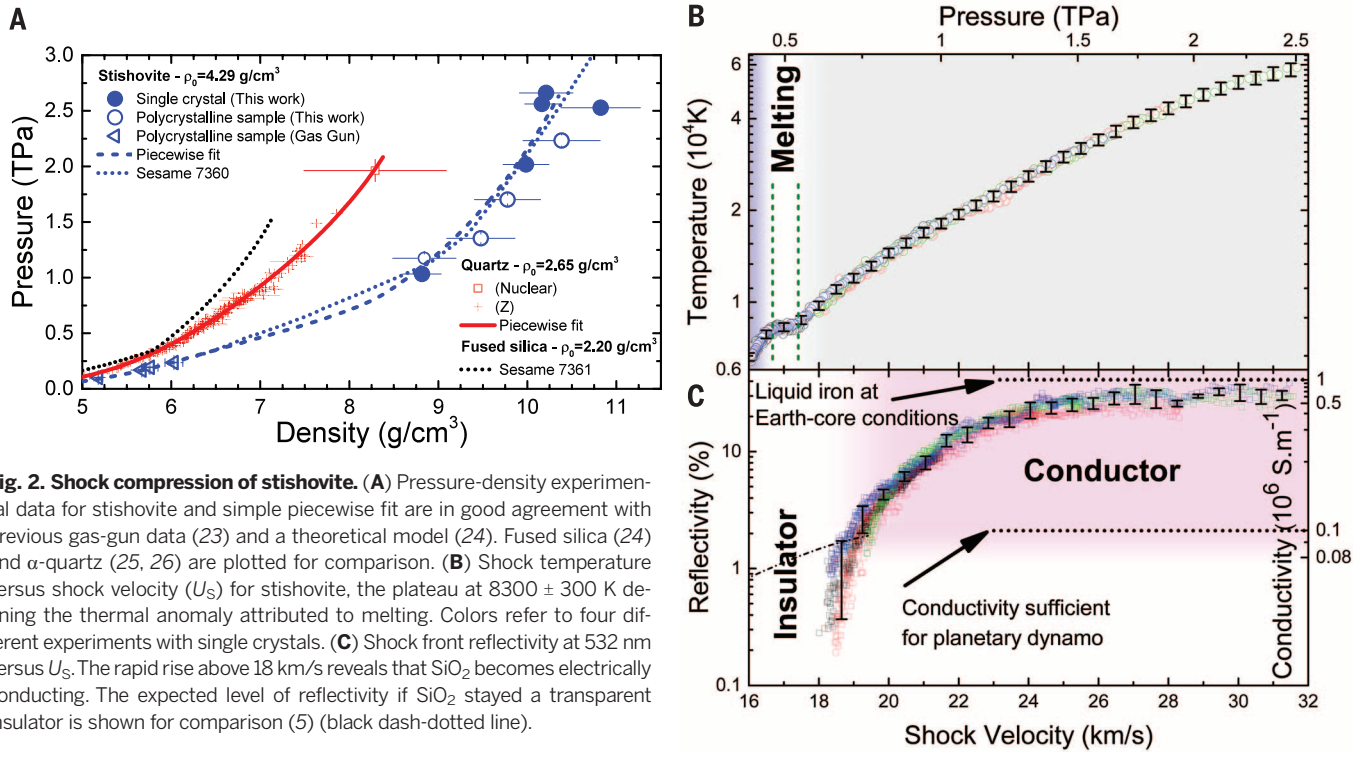

Fig. 2. Shock compression of stishovite. (**A**) Pressure-density experimental data for stishovite and simple piecewise fit are in good agreement with previous gas-gun data (*23*) and a theoretical model (*24*). Fused silica (*24*) and α-quartz (*25*, *26*) are plotted for comparison. (**B**) Shock temperature versus shock velocity (U_S) for stishovite, the plateau at 8300 ± 300 K defining the thermal anomaly attributed to melting. Colors refer to four different experiments with single crystals. (**C**) Shock front reflectivity at 532 nm versus U_S. The rapid rise above 18 km/s reveals that SiO_2 becomes electrically conducting. The expected level of reflectivity if SiO_2 stayed a transparent insulator is shown for comparison (*5*) (black dash-dotted line).

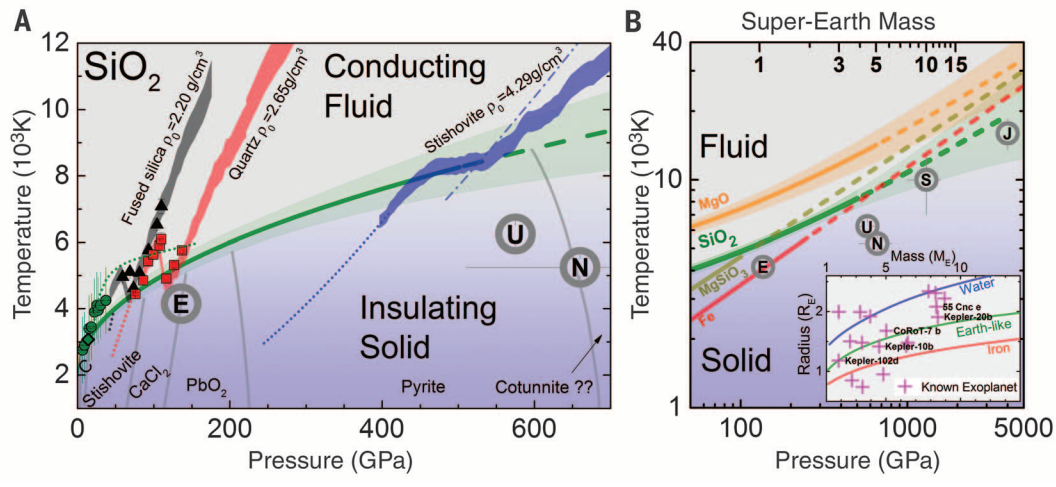

Fig. 3. Melting line of silica at planetary interior conditions determined by shock compression experiments. (**A**) The shock temperature plateau at 500 GPa reveals the crossing of the stishovite Hugoniot (blue) with the silica melting line. The data for α-quartz (red) and fused silica (gray) reproduce the strong temperature reversal upon melting observed with gas-gun experiments (*6*, *7*) (squares and triangles). A Simon fit of the shock and static compression data (*12*, *14*) (diamond, dots) provides a melting line up to TPa pressure (green line and shaded 1 σ uncertainty). Thick gray lines are known and predicted solid-phase boundaries (*27*). Dotted blue, red, and black lines are calculated Hugoniot curves below melting for stishovite (*5*), quartz (*8*), and fused silica (*24*). Predicted fluid properties are shown as the Hugoniot calculated from the ANEOS model (*17*) (blue dash-dotted) and the classical molecular dynamics melting line (*28*) (dotted green). (**B**) New experimental SiO_2 melting line and core mantle boundaries (gray circles) for Earth (E), Uranus (U) (*29*), Neptune (N) (*29*), Saturn (S) (*21*), and Jupiter (J) (*21*); melting lines of MgO, $MgSiO_3$, and Fe (dashed when extrapolated) (*5*) are shown for comparison. Top scale relates the pressure at the core-mantle boundary to the mass of Earth-like large exoplanets (*30*). (Inset) Discovered super-Earths and mass-radius relation for pure iron, water, or Earth-like structure that allow us to identify potentially rocky exoplanets (*5*).

into MgO and SiO_2 at TPa pressures (*20*). Solid cores in these planets would not participate in magnetic field generation and may be more resistant to erosion by the surrounding fluids (*21*).

Because rocky super-Earths are probably molten at the end of their accretion and many of them are expected to have high surface temperature, melting of silicates can regulate planetary evolution through control of internal heat flow. In particular, several mechanisms may tend to pin the core-mantle boundary temperature to the silicate melting line (*4*). If we overlook alloying effects and solidus-liquidus differences, our high-pressure measurements can thus be used to compare the melting behavior of silicates and iron alloys up to the terapascal range (Fig. 3 and fig. S14). As iron melts at lower temperature than silica up to ~0.6 TPa, an Earth-like structure with an iron-rich liquid outer core surrounded by a solid silicate mantle could subsist in a super-Earth up to ~5 Earth masses (M_E), such as exoplanets Kepler 102-d, Kepler 10 b, and Corot 7b (inset in Fig. 3B). In contrast, larger rocky exoplanets, like Kepler 20-b or 55 Cnc e, would likely have an extended basal magma ocean in the lower mantle that could affect their magnetic field and reinforce tidal response (*22*).

We find that molten silicate deep within large planetary mantles, in general, can contribute to magnetic field generation like the iron-rich liquid in the planetary cores. Magnetic fields provide information about the interior dynamics of planets and are potentially observable for exoplanets. Our discovery of conductive liquid silica at high pressures suggests a need to investigate planetary structure models that include multiple layers of conductive fluids.

REFERENCES AND NOTES

1. G. F. Davies, *Geophys. Res. Lett.* **9**, 1267–1270 (1982).
2. R. M. Canup, *Science* **338**, 1052–1055 (2012).
3. L. T. Elkins-Tanton, *Annu. Rev. Earth Planet. Sci.* **40**, 113–139 (2012).
4. L. Stixrude, *Philos. Trans. A. Math. Phys. Eng. Sci.* **372**, 20130076 (2014).
5. Materials and methods are available as supplementary materials on *Science* Online.
6. G. A. Lyzenga, T. J. Ahrens, A. C. Mitchell, *J. Geophys. Res.* **88** (B3), 2431 (1983).
7. M. B. Boslough, *J. Geophys. Res.* **93**(B6), 6477 (1988).
8. S.-N. Luo, T. J. Ahrens, P. D. Asimow, *J. Geophys. Res.* **108** (B9), 2421 (2003).
9. D. G. Hicks *et al.*, *Phys. Rev. Lett.* **97**, 025502 (2006).
10. R. McQueen, *Shock Compression of Condensed Matter–1991* (Elsevier, Amsterdam, 1992).
11. D. G. Hicks *et al.*, *Phys. Plasmas* **12**, 082702 (2005).
12. G. Shen, P. Lazor, *J. Geophys. Res.* **100** (B9), 17699 (1995).
13. F. Wang, Y. Tange, T. Irifune, K.-i. Funakoshi, *J. Geophys. Res.* **117**(B6) (2012) 10.1029/2011JB009100.
14. J. Zhang, R. C. Liebermann, T. Gasparik, C. T. Herzberg, Y. Fei, *J. Geophys. Res.* **98**(B11), 19785 (1993).
15. M. Pozzo, C. Davies, D. Gubbins, D. Alfè, *Nature* **485**, 355–358 (2012).
16. D. J. Stevenson, *Space Sci. Rev.* **152**, 651–664 (2010).
17. H. J. Melosh, *Meteorit. Planet. Sci.* **42**, 2079–2098 (2007).
18. J. H. Eggert *et al.*, *Nat. Phys.* **6**, 40–43 (2009).
19. R. S. McWilliams *et al.*, *Science* **338**, 1330–1333 (2012).
20. K. Umemoto, R. M. Wentzcovitch, P. B. Allen, *Science* **311**, 983–986 (2006).
21. F. González-Cataldo, H. F. Wilson, B. Militzer, *Astrophys. J.* **787**, 79 (2014).
22. Y. Harada *et al.*, *Nat. Geosci.* **7**, 569–572 (2014).
23. S.-N. Luo, *J. Geophys. Res.* **109**(B5), B05205 (2004).
24. G. I. Kerley, "Equations of state for composite materials" (Report KPS99-4, Kerley Publishing Services, 1999).
25. R. Trunin, *Physics-Uspekhi* **37**, 1123–1145 (1994).
26. M. D. Knudson, M. P. Desjarlais, *Phys. Rev. B* **88**, 184107 (2013).
27. T. Tsuchiya, J. Tsuchiya, *Proc. Natl. Acad. Sci. U.S.A.* **108**, 1252–1255 (2011).
28. A. B. Belonoshko, L. S. Dubrovinsky, *Geochim. Cosmochim. Acta* **59**, 1883–1889 (1995).
29. N. Nettelmann, R. Helled, J. Fortney, R. Redmer, *Planet. Space Sci.* **77**, 143–151 (2013).
30. F. W. Wagner, N. Tosi, F. Sohl, H. Rauer, T. Spohn, *Astron. Astrophys.* **541**, A103 (2012).

ACKNOWLEDGMENTS

Data are available in the supplementary materials and upon request to millot1@llnl.gov. Authors gratefully acknowledge assistance of A. Correa Barrios, W. Unites, R. Wallace, C. Davis, and J. Emig, Lawrence Livermore National Laboratory (LLNL); R. Paguio, M. Farrell, and A. Nikroo, General Atomics; M. Bonino, D. Harding, and the entire Omega Laser staff at the Laboratory for Laser Energetics (LLE); H. Schulze, T. Boffa Ballaran, A. Audetat, and H. Fischer (Bayreuth University); and discussions with D. K. Spaulding, T. R. Boehly, and J. R. Rygg. Prepared by LLNL under contract DE-AC52-07NA27344. Omega shots were allocated by LLE Laboratory Basic Science program. N.D. thanks the German Research Foundation (Deutsche Forschungsgemeinschaft, DFG) and the Federal Ministry of Education and Research (BMBF, Germany) for financial support through the DFG Heisenberg Program and project no. DU 954-8/1 and the BMBF grant no. 5K13WC3 (Verbundprojekt 05K2013, Teilprojekt 2, PT-DESY). Partial support was provided by the U.S. Department of Energy and the University of California, including UC Berkeley's Miller Institute for Basic Research in Science.

SUPPLEMENTARY MATERIALS

www.sciencemag.org/content/347/6220/418/suppl/DC1
Materials and Methods
Figures S1 to S15
Tables S1 to S3
References (*31*–*75*)

22 September 2014; accepted 19 December 2014
10.1126/science.1261507

MAGNETIC MATERIALS

Tilt engineering of spontaneous polarization and magnetization above 300 K in a bulk layered perovskite

Michael J. Pitcher,[1] Pranab Mandal,[1] Matthew S. Dyer,[1] Jonathan Alaria,[2] Pavel Borisov,[1]* Hongjun Niu,[1] John B. Claridge,[1]† Matthew J. Rosseinsky[1]†

Crystalline materials that combine electrical polarization and magnetization could be advantageous in applications such as information storage, but these properties are usually considered to have incompatible chemical bonding and electronic requirements. Recent theoretical work on perovskite materials suggested a route for combining both properties. We used crystal chemistry to engineer specific atomic displacements in a layered perovskite, $(Ca_ySr_{1-y})_{1.15}Tb_{1.85}Fe_2O_7$, that change its symmetry and simultaneously generate electrical polarization and magnetization above room temperature. The two resulting properties are magnetoelectrically coupled as they arise from the same displacements.

For many technical applications, crystalline solids must combine distinct properties. For example, in thermoelectrics, thermal and electronic conductivity need to be optimized simultaneously (*1*). This level of structure-property-composition control is particularly difficult when the properties have antagonistic chemical requirements. For example, the synthesis of a single phase combining electrical polarization P and spontaneous magnetization M is challenging to achieve because of the distinct electronic structure requirements for the main mechanisms producing each property (*2*); for example, the closed-shell d^0 Ti^{4+} and s^2 Pb^{2+} cations, which produce polarization in the ferroelectric perovskite oxide $PbZr_{1-x}Ti_xO_3$, do not have the unpaired electrons needed for magnetization (*3*). Efficiently combining these two long-range orders could be useful for multiferroic or magnetoelectric (ME) information storage, which could overcome the drawbacks of ferroelectric memory (slow writing) and magnetic random access memory (high power density) and open the possibility of four-state memory (*4*, *5*) with reduced energy consumption. It is possible to combine these ground states by making composites over a range of length scales between phases that individually have the chemistry and, thus, properties required (*6*, *7*) or by lowering spatial symmetry through the onset of magnetic order at low temperatures (*8*). We use chemical control of the crystal structure of a single-phase material to generate atomic displacements that produce both properties simultaneously in a coupled manner above room temperature (RT).

The chemical incompatibility between P and M arises when the ferroelectricity is driven by a classical gamma point instability (*9*). Recent theoretical work (*10*, *11*) has identified that specific zone-boundary octahedral tilts in an ABO_3

[1]Department of Chemistry, University of Liverpool, Crown Street, Liverpool L69 7ZD, UK. [2]Department of Physics, University of Liverpool, Liverpool L69 7ZE, UK.
*Present address: Department of Physics, West Virginia University, P.O. Box 6315, Morgantown, WV 26506, USA. †Corresponding author. E-mail: m.j.rosseinsky@liv.ac.uk (M.J.R.); j.b.claridge@liv.ac.uk (J.B.C.)

Shock compression of stishovite and melting of silica at planetary interior conditions

M. Millot *et al.*

Science **347**, 418 (2015);
DOI: 10.1126/science.1261507